Neutral-current supernova neutrino-nucleus scattering off ^{127}I and ^{133}Cs

Matti Hellgren [*] and Jouni Suhonen [†]
University of Jyväskylä, Department of Physics, P.O. Box 35 (YFL), Jyväskylä FI-40014, Finland

(Received 3 May 2022; accepted 22 July 2022; published 31 August 2022)

A large number of the presently running neutrino and dark-matter experiments use thallium-doped cesium-iodide CsI[Tl] crystals, sodium-doped cesium-iodide CsI[Na] crystals, or thallium-doped sodium-iodide NaI[Tl] crystals. In the present paper we calculate elastic and inelastic cross sections for neutral-current supernova-neutrino scattering off ^{127}I and ^{133}Cs, relevant for experiments using CsI[Tl], CsI[Na], or NaI[Tl] crystals. We study also the cross sections folded with two-parameter Fermi-Dirac distributions of the supernova-neutrino spectrum. The adopted nuclear-theory framework is the microscopic quasiparticle-phonon model, able to operate in large single-particle valence bases and use G-matrix based two-nucleon interactions with a phenomenological renormalization.

DOI: 10.1103/PhysRevC.106.025808

I. INTRODUCTION

Supernovae emit neutrinos (ν) and antineutrinos ($\bar{\nu}$) of all flavors: electron (e), muon (μ), and tau (τ). These (anti)neutrinos have their own characteristic energy distributions, which are usually described by a modified Fermi-Dirac distribution parametrized by the (anti)neutrino temperature and the pinching parameter. (Anti)neutrinos are produced in large quantities, e.g., in core-collapse type II supernova explosions [1,2], and nuclear responses to them [3–5] govern the feasibility of their detection. Detection of these neutrinos is of paramount importance since they are probes of physics beyond the standard model [6,7], supernova mechanisms [8,9], and nucleosynthesis of heavy elements [10,11]. The calculation of (anti)neutrino scattering cross sections constitutes an important tool for separating the different (anti)neutrino flavors and exploring the deep nature of weak interactions [12,13]. These cross sections are sensitive to the details of nuclear structure, e.g., locations of giant resonances.

Supernova (anti)neutrinos of all flavors can interact with atomic nuclei via an exchange of the neutral Z^0 boson in what is known as a neutral-current (NC) neutrino-nucleus scattering, and can thus be detected in experiments. Charged-current scattering, on the other hand, is experimentally relevant only for supernova electron (anti)neutrinos, as the relevant energy range of these (anti)neutrinos ($\lesssim$80 MeV) is below the thresholds of μ and τ production [13]. Numerous detectors capable of supernova detection are running, under construction or in a planning stage [14]. A network of detectors known as the SuperNova Early Warning System (SNEWS) [15] is also currently running. The goal of this system is to detect supernova (anti)neutrinos originating from new supernovae in the Milky Way or another nearby galaxy before the visible light photons from such event reach Earth, thus providing an early warning for astronomers. SNEWS has been running on automated mode since 2005, and the neutrino experiments that currently take part in it are Super-Kamiokande [16], LVD [17], Ice Cube [18], KamLAND [19], Borexino [20], HALO [21], and KM3NeT [22].

There are also detectors for solar neutrinos, accelerator neutrinos, geoneutrinos, reactor neutrinos, etc. [23], and neutrinos can also be detected by dark-matter detectors [24]. Very many of these detectors use thallium-doped cesium-iodide CsI[Tl] crystals, like the KIMS [25] experiment, or sodium-doped cesium-iodide CsI[Na] crystals, like the COHERENT [26] experiment. Many experiments use also thallium-doped sodium-iodide NaI[Tl] crystals, like KIMS [27], DAMA/LIBRA [28], DM-Ice [29], PICO-LON [30], SABRE [31], and ANAIS [32]. In this paper we calculate cross sections for NC supernova-neutrino scattering off ^{127}I and ^{133}Cs, relevant for experiments using CsI[Tl], CsI[Na], or NaI[Tl] crystals.

Neutral-current neutrino-nucleus scattering cross sections have been previously computed for isotopes of a number of intermediate mass ($50 \leqslant A \leqslant 150$) nuclei, including ^{56}Fe [33–37], ^{56}Ni [33,34], ^{64,66}Zn [38], ^{82}Ge [37], ^{93}Nb [39], $^{92,94-98,100}$Mo [34,40–44], ^{99}Ru [39], $^{106,108,110-114,116}$Cd [45], ^{128,130}Te [46], $^{128-132,134,136}$Xe [47,48], and ^{138}La [49]. In addition to these, corresponding calculations have also been performed for light and heavy nuclei including ^{4}He [50,51], ^{12}C [33,34,51–53], ^{16}O [34,52,53], ^{40}Ar [54], ^{180}Ta [49], and ^{204,206,208}Pb [35,55–57]. In many of the previous calculations, the theoretical nuclear structure data have been obtained by utilizing the nuclear-theory framework coined the microscopic quasiparticle-phonon model (MQPM) [58]. We use MQPM also in this paper in order to compute the scattering cross sections as functions of the energy of the incoming neutrino. We also provide estimates of total folded cross sections for supernova (anti)neutrinos modeled by a modified Fermi-Dirac energy distribution parametrized by

[*] majokahe@jyu.fi
[†] jouni.t.suhonen@jyu.fi

the (anti)neutrino temperature and the pinching parameter. The MQPM is based on the quasiparticle random-phase approximation (QRPA) theory, where the QRPA is used to describe the excitations (phonons) of the even-even reference nuclei. These phonons are subsequently coupled with Bardeen-Cooper-Schrieffer (BCS) quasiparticles in order to describe the one- and three-quasiparticle excitations in odd-even and even-odd nuclei, like in ^{127}I and ^{133}Cs. In this paper we use, for the first time, two reference nuclei on par with each other to describe the structure of the ^{127}I and ^{133}Cs nuclei. Based on this, we give the scattering results using both references in order to access the magnitude of the effect of using different reference nuclei in the MQPM calculations.

The paper is organized as follows: In Sec. II we outline the used nuclear-structure method and discuss its application and the produced spectra for the nuclei relevant for this paper. In addition, we briefly review the adopted scattering formalism. In Sec. III we give the results for the folded and unfolded scattering cross sections, and in Sec. IV the conclusions are drawn.

II. THEORY

A. Nuclear structure

The wave functions for the nuclei of interest used in the neutrino scattering calculations were obtained by utilizing MQPM. MQPM is based on the QRPA, which is, in turn, based the BCS model for the atomic nucleus. Given a set of particle- and hole-creation operators $c^\dagger_\alpha$ and $\tilde{c}_\alpha$ with quantum numbers $\alpha \equiv (a, m_\alpha) \equiv (n_a, l_a, j_a, m_\alpha)$, l_a being the orbital angular momentum, j_a the total angular momentum, m_α its z projection, and n_a the radial quantum number, the BCS quasiparticles are defined by the Bogolyubov-Valatin transformation:

$$a^\dagger_\alpha = u_a c^\dagger_\alpha + v_a \tilde{c}_\alpha, \quad \tilde{a}_\alpha = u_a \tilde{c}_\alpha - v_a c^\dagger_\alpha, \tag{1}$$

where the parameters u_a and v_a are the occupation amplitudes of the orbital α. The BCS calculations were performed on an even-even reference nucleus adjacent to the nucleus of interest by fitting the lowest quasiparticle energies of both nucleon species to the experimental pairing gaps $\Delta_{\pi(\nu)}$. For the pairing gaps, the three-point formulas

$$\Delta_\pi = \tfrac{1}{4}(-1)^{Z+1}(S_p(A+1, Z+1) - 2S_p(A, Z) + S_p(A-1, Z-1)) \tag{2}$$

and

$$\Delta_\nu = \tfrac{1}{4}(-1)^{N+1}(S_n(A+1, Z) - 2S_n(A, Z) + S_n(A-1, Z)), \tag{3}$$

where $S_{p(n)}$ is the experimental proton (neutron) separation energy, were used. The single-particle states used were obtained by solving the Coulomb corrected Woods-Saxon single-particle Hamiltonian with Bohr-Mottelson parametrization [59]. The energies of the single-particle states near the Fermi surface were adjusted prior to the BCS calculation to improve the agreement between the QRPA spectra and corresponding experimental results. These adjustments are presented in Table I.

TABLE I. Adjustments to the energies of the single-particle Woods-Saxon orbitals for all MQPM reference nuclei (MeV).

Orbital	^{126}Te	^{128}Xe	^{132}Xe	^{134}Ba
$1d_{5/2,\pi}$				+0.03
$0g_{7/2,\pi}$	−0.15	−0.20	−0.35	−0.70
$0h_{11/2,\pi}$	−0.60	−0.30	−0.60	−0.50
$2s_{1/2,\pi}$				
$1d_{3/2,\pi}$				
$1d_{5/2,\nu}$				
$0g_{7/2,\nu}$	+1.00	+2.00		
$2s_{1/2,\nu}$	+0.90	+0.60	+0.30	+1.00
$1d_{3/2,\nu}$	+0.60	−0.30	+0.50	+0.14
$0h_{11/2,\nu}$	−1.00	−1.13	−1.00	−1.00

The next step after the BCS calculations was to construct the QRPA phonon operators

$$Q^\dagger_\omega = \sum_{a\leqslant b}\left[X^\omega_{ab}A^\dagger_{ab}(JM) - Y^\omega_{ab}\tilde{A}_{ab}(JM)\right] \tag{4}$$

by coupling two quasiparticle creation operators to a definite angular momentum. The amplitudes X^ω_{ab} and Y^ω_{ab} were determined by solving the QRPA equations:

$$\begin{pmatrix} \mathsf{A} & \mathsf{B} \\ -\mathsf{B}^* & -\mathsf{A}^* \end{pmatrix}\begin{pmatrix} \mathsf{X}^\omega \\ \mathsf{Y}^\omega \end{pmatrix} = E_\omega \begin{pmatrix} \mathsf{X}^\omega \\ \mathsf{Y}^\omega \end{pmatrix}. \tag{5}$$

The operator $Q^\dagger_\omega$ was then used to generate the QRPA one-phonon excited states:

$$|Q_\omega\rangle = Q^\dagger_\omega |\mathrm{QRPA}\rangle\,. \tag{6}$$

In the above equations [60]

$$\begin{aligned} A^\dagger_{ab}(JM) &= \mathcal{N}_{ab}(J)[a^\dagger_a a^\dagger_b]_{JM}, \\ \tilde{A}_{ab}(JM) &= (-1)^{J+M}A_{ab}(J-M), \\ \mathcal{N}_{ab}(J) &= \frac{\sqrt{1+\delta_{ab}(-1)^J}}{1+\delta_{ab}}, \end{aligned} \tag{7}$$

A is the quasiparticle Tamm-Dancoff approximation matrix, $|\mathrm{QRPA}\rangle$ the correlated QRPA ground state, and B the correlation matrix. Of the quantum numbers $\omega \equiv \{J_\omega, \pi_\omega, k_\omega\}$ of an excited state, the first two characterize the angular momentum and parity of the state, respectively, while the third enumerates the phonons.

The QRPA equations were solved in a one-phonon basis for each even-even reference nucleus by fitting the results to experimental spectra for each natural multipolarity up to and including 6^+. This was achieved by scaling the two-body matrix elements of a given multipolarity J^π, appearing in matrices A and B with phenomenological particle-particle and particle-hole strength parameters g_{pp} and g_{ph} [61,62]. The values used for these parameters are presented in Tables II and III. The fitting procedure itself consisted of adjusting the g_{ph} values so that the energies of the lowest theoretical states matched the corresponding experimental states, with two exceptions.

First, the computed lowest excited 0^+ state is spurious, and its energy was set as close to zero as possible, and the

TABLE II. Values used for the phenomenological particle-hole strength parameters for each multipolarity for all even-even reference nuclei. The default value of 1.00 was used for all states of unnatural multipolarity, for all nuclei involved.

Nucleus	0^+	1^-	2^+	3^-	4^+	5^-	6^+
^{126}Te	0.3179	0.5	0.4941	0.6090	0.362	0.7125	0.8560
^{128}Xe	0.2576	0.5	0.4543	0.6047	0.556	0.5775	0.8684
^{132}Xe	0.3265	0.5	0.5123	0.6043	0.520	0.8492	0.5450
^{134}Ba	0.3254	0.5	0.5037	0.6415	0.560	0.7720	0.6955

theoretical second excited 0^+ was instead fitted to the experimental first excited 0^+ state. This was achieved by adjusting both the particle-hole and the particle-particle strength parameters, which was in contrast with the fits for the rest of the multipoles, for which g_{pp} was unmodified from its default value. Secondly, only single-phonon QRPA states as given by Eq. (6) were considered in this paper. Operators that generate multiphonon states can be similarly constructed by coupling two or more phonon operators to a definite angular momentum. In particular, coupling two quadrupole phonons in this way generates a triplet of 0^+, 2^+, and 4^+ states theoretically degenerate in energy [60]. For all even-even nuclei considered in this paper, the lowest experimental 4^+ and second lowest 2^+ states exhibit signs that these states contain considerable two-phonon components. Based on this, the lowest theoretical 4^+ was fitted to the second lowest experimental 4^+ for all even-even nuclei. The resulting theoretical spectra, compared to the experimental spectra [63–66], are illustrated in Figs. 1 and 2.

After solving the QRPA equations, the MQPM excitation creation operators

$$\Gamma_i^\dagger(JM) = \sum_n C_n^i a_{nJM}^\dagger + \sum_{a\omega} D_{a\omega}^i [a_a^\dagger Q_\omega^\dagger]_{JM} \tag{8}$$

TABLE III. Values used for the phenomenological particle-particle strength parameters for the multipolarity 0^+ for all even-even reference nuclei. The default value of 1.00 was used for all other multipolarities.

	^{126}Te	^{128}Xe	^{132}Xe	^{134}Ba
g_{pp} for 0^+	0.6100	0.6992	0.6590	0.7031

were constructed by solving the MQPM equations

$$\begin{pmatrix} A & B \\ B^{\mathrm{T}} & A' \end{pmatrix} \begin{pmatrix} C^i \\ D^i \end{pmatrix} = \Omega_i \begin{pmatrix} 1 & 0 \\ 0 & N \end{pmatrix} \begin{pmatrix} C^i \\ D^i \end{pmatrix} \tag{9}$$

for the amplitudes C_n^i and $D_{a\omega}^i$ [58]. As can be seen from Eq. (8), the MQPM states are made up of quasiparticle and quasiparticle-phonon components. The MQPM equations and the submatrices A, A', B, and N are discussed in detail in [58]. The same values for the g_{ph} and g_{pp} parameters were used in the MQPM calculations as in the QRPA calculations. As no new fitting parameters were introduced in the MQPM calculations, all fitting to experimental data was done during the BCS and QRPA calculations. The aforementioned spurious 0^+ state was excluded from the MQPM calculations along with the first 1^- state, which is contaminated by contributions arising from unphysical center of mass motion of the nucleus about the origin of the coordinate system. The resulting theoretical spectra, compared to the corresponding experimental spectra [67,68], are presented in Figs. 3 and 4.

B. Neutrino scattering

A standard-model neutral-current neutrino-nucleus scattering process

$$N(A,Z) + \nu \rightarrow N(A,Z)^* + \nu \tag{10}$$

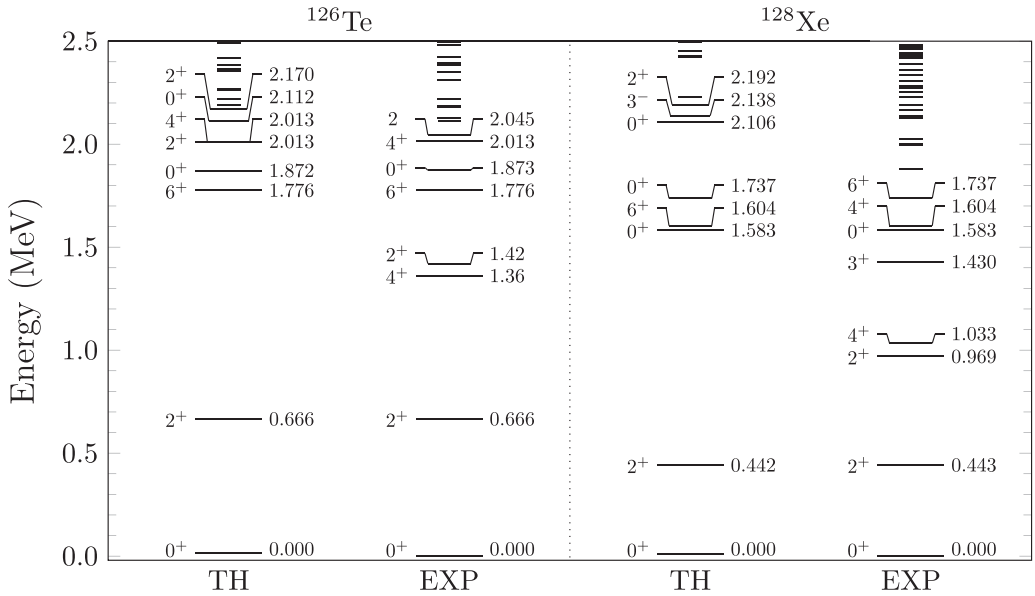

FIG. 1. Experimental [63,64] and QRPA-computed energy spectra of ^{126}Te (left) and ^{126}Xe (right).

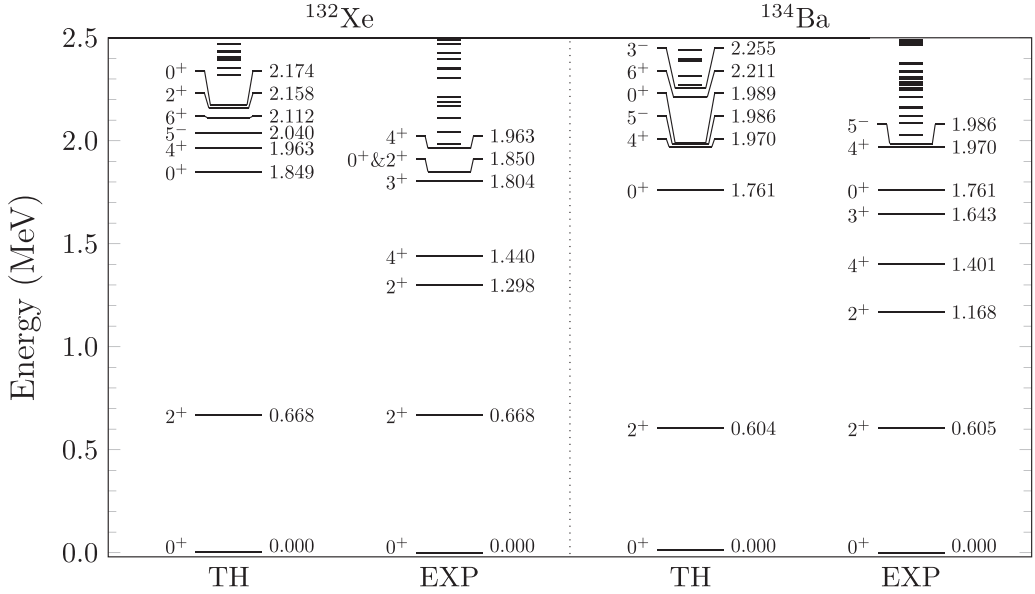

FIG. 2. Experimental [65,66] and QRPA-computed energy spectra of ^{132}Xe (left) and ^{134}Ba (right).

proceeds through the exchange of a neutral Z^0 boson of mass M_Z. The kinematics of this reaction are illustrated in Fig. 5. The final state of the nucleus $N(A, Z)^*$ can be the same as the initial state $N(A, Z)$ prior to the reaction in the case of elastic scattering, or an excited state in the case of inelastic scattering. As the transferred four-momentum $q_\mu = k'_\mu - k_\mu$ fulfils

$$M_Z^2 \gg -q_\mu q^\mu \equiv Q^2, \tag{11}$$

the process can be treated in the lowest order as a pointlike current-current interaction with an effective Hamiltonian:

$$H_{\text{eff}} = \frac{G}{\sqrt{2}} \int d^3\mathbf{x}\, j_\mu(\mathbf{x}) \mathcal{J}^\mu(\mathbf{x}), \tag{12}$$

where $\mathcal{J}^\mu(\mathbf{x})$ and $j_\mu(\mathbf{x})$ are the nuclear and lepton currents, respectively, and $G = 1.1664 \times 10^{-5}$ GeV. The matrix element of the effective Hamiltonian can then be expressed as

$$\langle f|H_{\text{eff}}|i\rangle = \frac{G}{\sqrt{2}} \int d^3 l_\mu e^{-i\mathbf{q}\cdot\mathbf{x}} \langle f|\mathcal{J}^\mu(\mathbf{x})|i\rangle\,, \tag{13}$$

where

$$l_\mu \equiv (l_0, -\mathbf{l}) = \langle f|j_\mu(\mathbf{x})|i\rangle\, e^{i\mathbf{q}\cdot\mathbf{x}} \tag{14}$$

is the lepton matrix element.

The double-differential cross section for the scattering of a (anti)neutrino and a nucleus in initial and final nuclear states $|J_{i/f}\rangle$, with $E_{\text{exc}} = E_f - E_i$, can then be shown to be

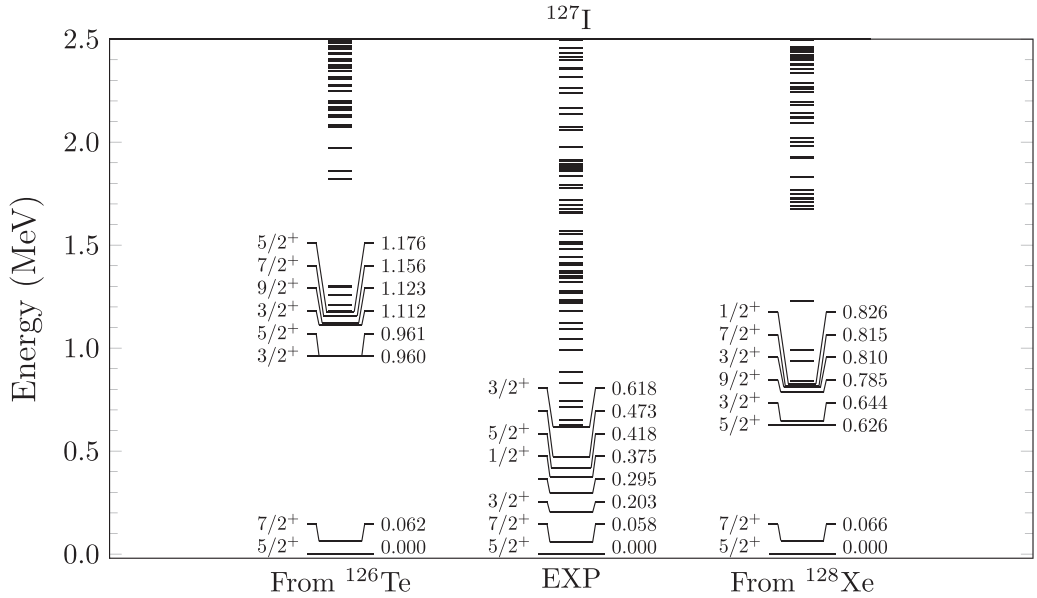

FIG. 3. Experimental [67] and MQPM-computed energy spectra of ^{127}I from the reference nuclei ^{126}Te (left) and ^{128}Xe (right).

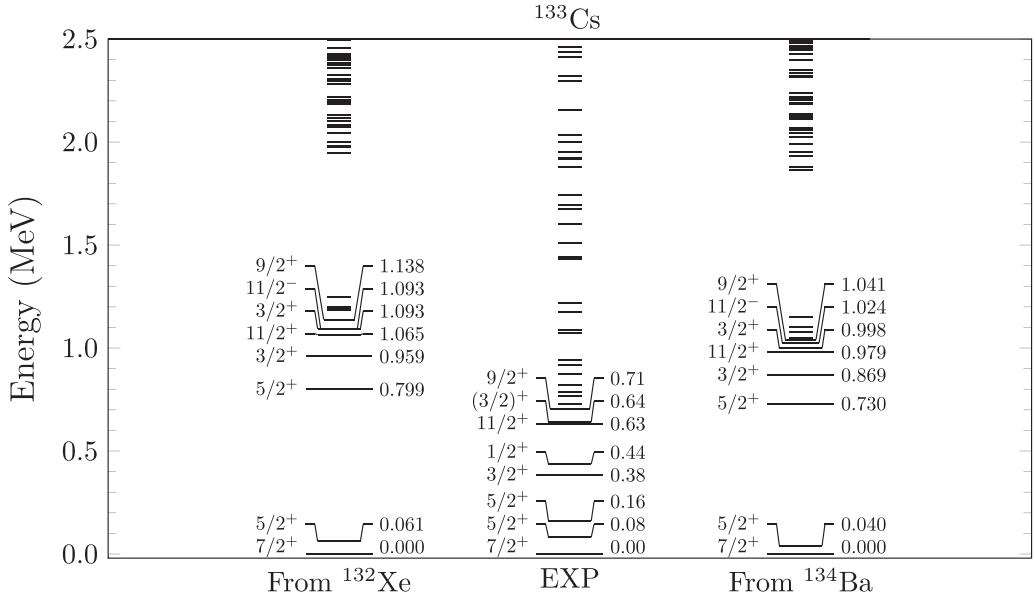

FIG. 4. Experimental [68] and MQPM-computed energy spectra of ^{133}Cs from the reference nuclei ^{132}Xe (left) and ^{134}Ba (right).

given by [40]

$$\left[\frac{d^2\sigma_{i\to f}}{d\Omega dE_{\rm exc}}\right]_{\nu/\bar{\nu}} = \frac{G^2|\mathbf{k}'|E_{\mathbf{k}'}}{\pi(2J_i+1)}\left(\sum_{J\geqslant 0}\sigma^J_{\rm CL}+\sum_{J\geqslant 1}\sigma^J_{\rm T}\right), \tag{15}$$

where $E_{\mathbf{k}/\mathbf{k}'}$ is the energy of the incoming/outgoing lepton with three-momentum $\mathbf{k}/\mathbf{k}'$, and

$$\sigma^J_{\rm CL} = (1+\cos\theta)|(J_f||\mathcal{M}_J(q)||J_i)|^2 + \left(1+\cos\theta-2\frac{E_{\mathbf{k}}E_{\mathbf{k}'}}{q^2}\sin^2\theta\right)|(J_f||\mathcal{L}_J(q)||J_i)|^2$$
$$+\frac{E_{\mathbf{k}}-E_{\mathbf{k}'}}{q}(1+\cos\theta)2{\rm Re}[(J_f||\mathcal{L}_J(q)||J_i)(J_f||\mathcal{M}_J(q)||J_i)^*] \tag{16}$$

and

$$\sigma^J_{\rm T} = \left(1-\cos\theta+\frac{E_{\mathbf{k}'}E_{\mathbf{k}}}{q^2}\sin^2\theta\right)\left[|(J_f||\mathcal{T}^{\rm el}_J(q)||J_i)|^2+|(J_f||\mathcal{T}^{\rm mag}_J(q)||J_i)|^2\right]$$
$$\mp\frac{(E_{\mathbf{k}}+E_{\mathbf{k}'})}{q}(1-\cos\theta)2{\rm Re}\left[(J_f||\mathcal{T}^{\rm mag}_J(q)||J_i)(J_f||\mathcal{T}^{\rm el}_J(q)||J_i)^*\right] \tag{17}$$

are the Coulomb-longitudinal (CL) and transverse (T) contributions to the cross section, respectively. The $(+)-$ sign in Eq. (17) corresponds to (anti)neutrino scattering. In the above expressions

$$q\equiv|\mathbf{q}|=\sqrt{(E_{\mathbf{k}}-E_{\mathbf{k}'})^2+2E_{\mathbf{k}'}E_{\mathbf{k}}(1-\cos\theta)} \tag{18}$$

is the magnitude of the transferred three-momentum, θ is the scattering angle of the lepton, and $\mathcal{M}_{JM}$, $\mathcal{L}_{JM}$, $\mathcal{T}^{\rm el}_{JM}$, and $\mathcal{T}^{\rm mag}_{JM}$ are spherical tensor operators involved in the multipole decomposition of the hadron current. They are defined and discussed in detail in [40,69,70].

III. RESULTS

A. Reaction cross sections

The scattering cross sections as functions of neutrino energy were calculated by using the formalism presented in the previous chapter. We first computed the double differential cross section given in Eq. (15) and numerically integrated it over the scattering angle. After this we summed over the possible final nuclear states. In this paper we considered both elastic scattering, in which the final nuclear state is the same as the initial state (in this case the ground state), and inelastic scattering, where the final nuclear state is an excited state. Scattering reactions were considered for all three neutrino flavors for both nuclei of interest. The results have been tabulated in Table IV.

TABLE IV. Total elastic and inelastic neutrino (ν) and antineutrino ($\overline{\nu}$) scattering cross sections as functions of the energy of the incoming neutrino for both nuclei with all MQPM reference nuclei. The format in which the data are presented is $(R_1, R_2)(e_1, e_2)$, and the cross sections are obtained by $\sigma(E_k) = R_{1/2} \times 10^{e_{1/2}}$. Here R_1 is the result obtained by using ^{126}Te(^{132}Xe) and R_2 is the result obtained by using ^{128}Xe(^{134}Ba) as the MQPM reference for ^{127}I(^{133}Cs), and e_1 and e_2 are the corresponding exponents. If the exponents are the same, only one number is given. The units are 10^{-40} (10^{-46}) cm^2 for elastic (inelastic) cross sections.

	^{127}I			^{133}Cs		
$E_\mathbf{k}$ (MeV)	ν_{inel}	$\overline{\nu}_{\text{inel}}$	$\nu_{\text{el}}/\overline{\nu}_{\text{el}}$	ν_{inel}	$\overline{\nu}_{\text{inel}}$	$\nu_{\text{el}}/\overline{\nu}_{\text{el}}$
5.0	(1.09,1.27)(2)	(1.06,1.24)(2)	(5.17,5.15)(0)	(1.01,1.18)(1)	(9.81,1.16)(0,1)	(5.76,5.74)(0)
10.0	(4.51,2.99)(3)	(4.18,2.79)(3)	(2.03,2.02)(1)	(2.46,2.22)(3)	(2.33,2.09)(3)	(2.25,2.25)(1)
15.0	(4.55,3.56)(4)	(4.21,3.32)(4)	(4.40,4.39)(1)	(4.19,3.72)(4)	(3.97,3.51)(4)	(4.89,4.88)(1)
20.0	(1.63,1.44)(5)	(1.48,1.33)(5)	(7.46,7.43)(1)	(1.53,1.36)(5)	(1.43,1.27)(5)	(8.28,8.26)(1)
25.0	(3.66,3.44)(5)	(3.26,3.08)(5)	(1.10,1.09)(2)	(3.51,3.13)(5)	(3.19,2.85)(5)	(1.22,1.21)(2)
30.0	(6.68,6.47)(5)	(5.78,5.64)(5)	(1.47,1.46)(2)	(6.49,5.83)(5)	(5.76,5.16)(5)	(1.63,1.62)(2)
35.0	(1.07,1.07)(6)	(9.06,9.01)(5)	(1.84,1.84)(2)	(1.06,9.58)(6,5)	(9.11,8.24)(5)	(2.04,2.03)(2)
40.0	(1.59,1.60)(6)	(1.31,1.31)(6)	(2.20,2.19)(2)	(1.58,1.45)(6)	(1.32,1.20)(6)	(2.42,2.42)(2)
45.0	(2.21,2.25)(6)	(1.77,1.79)(6)	(2.52,2.51)(2)	(2.21,2.04)(6)	(1.79,1.65)(6)	(2.78,2.77)(2)
50.0	(2.94,3.01)(6)	(2.29,2.33)(6)	(2.81,2.80)(2)	(2.92,2.73)(6)	(2.30,2.14)(6)	(3.08,3.07)(2)
55.0	(3.76,3.86)(6)	(2.85,2.92)(6)	(3.05,3.04)(2)	(3.71,3.51)(6)	(2.84,2.68)(6)	(3.34,3.33)(2)
60.0	(4.67,4.79)(6)	(3.46,3.54)(6)	(3.25,3.24)(2)	(4.56,4.36)(6)	(3.40,3.24)(6)	(3.56,3.55)(2)
65.0	(5.64,5.80)(6)	(4.09,4.19)(6)	(3.42,3.41)(2)	(5.44,5.25)(6)	(3.97,3.82)(6)	(3.74,3.73)(2)
70.0	(6.68,6.87)(6)	(4.74,4.88)(6)	(3.56,3.55)(2)	(6.37,6.18)(6)	(4.55,4.40)(6)	(3.88,3.87)(2)
75.0	(7.77,7.99)(6)	(5.40,5.58)(6)	(3.67,3.66)(2)	(7.32,7.14)(6)	(5.13,4.99)(6)	(4.00,3.98)(2)
80.0	(8.88,9.15)(6)	(6.06,6.29)(6)	(3.76,3.75)(2)	(8.29,8.12)(6)	(5.71,5.58)(6)	(4.09,4.08)(2)
85.0	(1.00,1.03)(7)	(6.71,7.01)(6)	(3.83,3.82)(2)	(9.28,9.10)(6)	(6.29,6.16)(6)	(4.17,4.16)(2)
90.0	(1.11,1.15)(7)	(7.34,7.72)(6)	(3.89,3.88)(2)	(1.03,1.01)(7)	(6.86,6.73)(6)	(4.24,4.22)(2)
95.0	(1.23,1.27)(7)	(7.95,8.41)(6)	(3.95,3.94)(2)	(1.13,1.10)(7)	(7.41,7.28)(6)	(4.29,4.28)(2)
100.0	(1.33,1.39)(7)	(8.53,9.08)(6)	(3.99,3.98)(2)	(1.22,1.20)(7)	(7.94,7.82)(6)	(4.34,4.33)(2)

The elastic neutrino and antineutrino scattering cross sections were almost identical, and only a single value computed using each individual reference nucleus is given for these two reactions for each neutrino energy. This is due to the fact that for elastic scattering the channel $J = 0$ dominates in Eq. (15). This is the $J = 0$ term of the Coulomb-longitudinal contribution of Eq. (16), which is identical for neutrino and antineutrino scattering. By comparing the elastic and inelastic cross sections it is clearly seen that the elastic cross sections are, expectedly, orders of magnitude larger than the corresponding inelastic cross sections. The relative differences between results obtained using different reference nuclei are also considerably more pronounced for inelastic scattering for all (anti)neutrino flavors. Overall, the agreement between inelastic scattering results from different reference nuclei is good for both nuclei.

Some of the results are also illustrated in Figs. 6 and 7. In the figures it can be seen that the elastic cross sections for ^{133}Cs are consistently larger than those of ^{127}I by roughly about a factor of $(133/127)^2$. The type of the neutrino (ν_e vs $\overline{\nu}_e$) is less important. This occurs for the entire range of neutrino energies considered. For inelastic scattering the situation is different. At low (<30 MeV) neutrino energies there is a noticeable difference between the cross sections for different nuclei, while the differences between cross sections for different neutrino types for both nuclei are minimal. At high energies this reverses and the cross sections for the two nuclei are nearly identical for the same neutrino types, and a difference between neutrino and antineutrino cross sections can be observed.

The dependence of the relative differences between the cross sections computed using different MQPM reference nuclei on the incoming neutrino energy was also investigated. We computed the percentual difference by dividing the difference of the two cross sections by their average for every neutrino energy in Table IV and plotted them in Fig. 8. The differences between the elastic results are both consistent throughout the entire neutrino energy range considered and extremely small, below 0.4% for both nuclei and both neutrino types. For the results of the inelastic scattering there is some variance between the percentual differences of the two

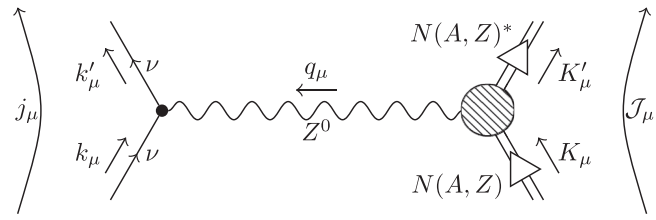

FIG. 5. Feynman diagram illustrating the interaction between a (anti)neutrino ν and an atomic nucleus $N(A, Z)$ via the exchange of a Z^0 boson. The four-momenta of the lepton and nucleus prior to the scattering are denoted by k_μ and K_μ, and after the scattering by k'_μ and K'_μ, respectively.

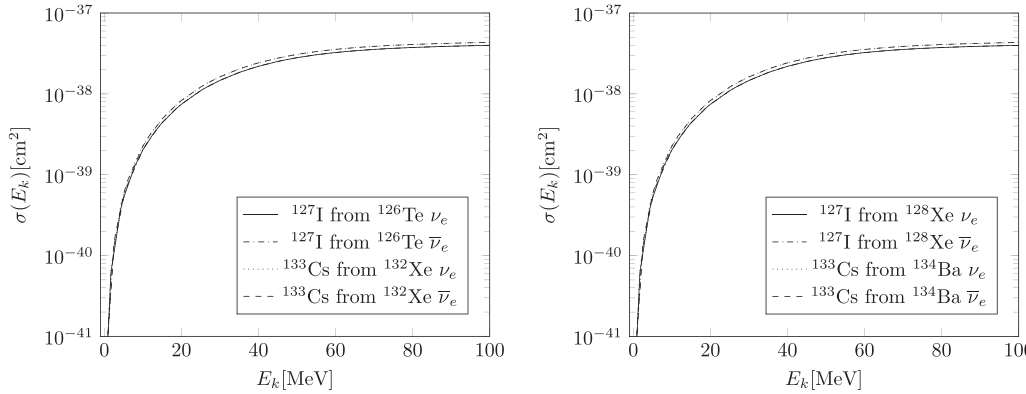

FIG. 6. Total elastic cross section as a function of neutrino energy for neutrino and antineutrino scattering off ^{127}I and ^{133}Cs. The MQPM reference nuclei used were ^{126}Te and ^{132}Xe (left) and ^{128}Xe and ^{134}Ba (right).

nuclei and between the percentual differences of one nucleus for different neutrino energies. The percentual differences for inelastic scattering are generally one or more orders of magnitude larger than the corresponding elastic ones. For neutrino energies below 20 MeV the percentual differences can exceed 10%, and in particular for ^{127}I the difference can be even some 40%. For higher neutrino energies the differences for ^{127}I are quite small, and also for ^{133}Cs less than 10%. There is practically no difference between the neutrino types. The large percentual differences at low neutrino energies come from the differences between the low-energy spectra of ^{127}I and ^{133}Cs generated using different reference nuclei: The low-energy neutrinos "feel" mainly the low-lying nuclear states. The differences between the two computed reference spectra are larger for ^{127}I (see the low-energy gaps in Figs. 1 and 2) explaining (partly) the larger percentual differences in the scattering cross section. In addition to the differences in excitation energy also the different decompositions of the wave functions of these states contribute to the percentual differences in the inelastic cross sections. As the neutrino energy increases and nuclear states higher in energy start to contribute more to the scattering cross section, the percentual differences decrease for both nuclei, as both reference nuclei produce similar overall features for the excitation spectrum and the differences from individual final states even out. This can also be seen in Fig. 8.

B. Folded cross sections

Cross section results for supernova neutrino-nucleus scattering were obtained by folding the cross section results of Table IV with energy spectra of supernova neutrinos. The supernova-neutrino model considered in this paper was based on a thermal Fermi-Dirac distribution with the energy distribution given by

$$p(E_\nu) = \frac{1}{T^3 F_2(\alpha)} \frac{E_\nu^2}{e^{E_\nu/T-\alpha}+1}, \tag{19}$$

where T is the effective neutrino temperature inside the supernova, and α is the degeneracy parameter which controls the pinching of the spectrum [71,72]. The Fermi-Dirac integral $F_2(\alpha)$, defined by

$$F_n(\alpha) = \int dx \frac{x^n}{1+e^{x-\alpha}}, \tag{20}$$

arises from normalization. Instead of the neutrino temperature T the distribution can be equivalently parametrized in terms of the average neutrino energy $\langle E_\nu \rangle$ which is related to the former

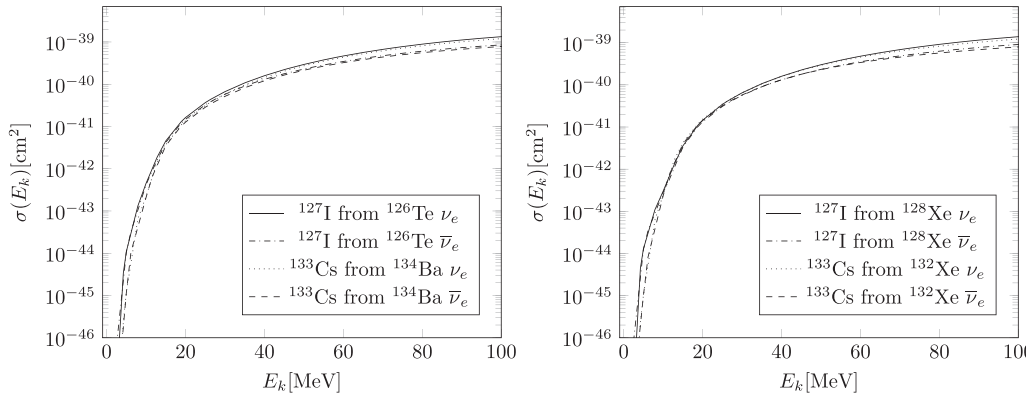

FIG. 7. Total inelastic cross section as a function of neutrino energy for neutrino and antineutrino scattering off ^{127}I and ^{133}Cs. The MQPM reference nuclei used were ^{126}Te and ^{134}Ba (left) and ^{128}Xe and ^{132}Xe (right).

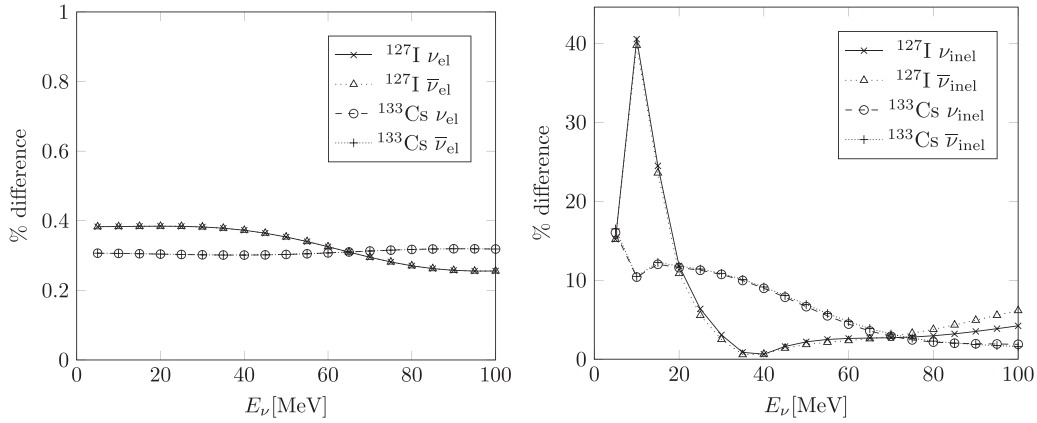

FIG. 8. The percentual differences between the cross sections of Table IV obtained for different reference nuclei. Results for elastic (inelastic) scattering are shown on the left (right).

according to

$$\langle E_\nu \rangle = \frac{F_2(\alpha)}{F_3(\alpha)} T. \tag{21}$$

Average neutrino energies used in this paper were adopted from [72], i.e., $\langle E_{\nu_e} \rangle = 11.0$ MeV, $\langle E_{\overline{\nu}_e} \rangle = 16.0$ MeV, and $\langle E_{\nu_x} \rangle = \langle E_{\overline{\nu}_x} \rangle = 25.0$ MeV. The corresponding neutrino temperatures have been tabulated in Table V. The total folded cross sections and the contributions to these from Coulomb-longitudinal and transverse terms from Eq. (15) are tabulated in Tables VI and VII, along with the contributions from terms of different tensorial character [vector (V), axial-vector (A), or interference (I)].

It can be seen in the tables that the folded cross sections and the individual contributions are somewhat sensitive to the neutrino temperature, especially the inelastic cross sections. The results obtained using different reference nuclei also vary more for inelastic scattering when compared to elastic scattering, which is expected based on the unfolded results presented earlier. The agreement between total folded cross sections from different reference nuclei is generally good overall. The differences between them reflect the differences in the unfolded cross sections discussed above. There is also considerable variance between the CL and T contributions, and between the V, A, and I contributions for elastic scattering. This variance is observed for both nuclei, and is explained by the fact that for elastic scattering the 0^+ multipole channel strongly dominates. The T contribution [Eq. (17)] contains multipoles with $J \geqslant 1$, and thus the CL contribution [Eq. (16)], which contains a $J = 0$ part, is orders of magnitude larger than the T contribution. The differences between the tensorial contributions also stem from the dominance of the 0^+ channel. The spherical tensor operators $\mathcal{M}_{JM}$, $\mathcal{L}_{JM}$, $\mathcal{T}^{\rm el}_{JM}$, and $\mathcal{T}^{\rm mag}_{JM}$ that make up the CL and T terms can be decomposed into vector and axial-vector parts according to [70]

$$\mathcal{O}_{JM}(q) = O^{\rm V}_{JM}(q) - O^{\rm A}_{JM}(q), \tag{22}$$

where ($O^{\rm A}_{JM}$) $O^{\rm V}_{JM}$ is a (axial-vector) vector operator. The operators $M^{\rm V}_{JM}$, $L^{\rm V}_{JM}$, $T^{\rm el,V}_{JM}$, and $T^{\rm mag,A}_{JM}$ have parity $(-1)^J$, while the operators $M^{\rm A}_{JM}$, $L^{\rm A}_{JM}$, $T^{\rm el,A}_{JM}$, and $T^{\rm mag,V}_{JM}$ have parity $(-1)^{J+1}$ [69]. Therefore only the operators $M^{\rm V}_{00}$ and $L^{\rm V}_{00}$ contribute in a 0^+ transition, and the V contribution is orders of magnitude larger than the A and I contributions.

To analyze further the folded scattering cross sections, the contributions from individual final nuclear states in the case of inelastic scattering were also obtained. These are of particular importance experimentally, as they provide information on the excitation strength function and deexcitation spectrum of a nucleus after a scattering event. These contributions are presented in Figs. 9 and 10 for the case of electron-neutrino scattering with a degeneracy parameter choice $\alpha = 3.0$.

Figures 9 and 10 indicate that for both nuclei there are a few prominent contributions to the folded inelastic cross section. For ^{127}I the highest of these contributions consists of a group of peaks centered at 9.7 MeV for both reference nuclei, although the reference nucleus ^{126}Te produces another smaller peak with similar features at around 9 MeV, due to splitting of the corresponding excitation strength. For ^{133}Cs the gross features of excitation strength are the same for both reference nuclei, with the prominent peaks lying between 8.6 and 8.8 MeV. The states that form these peaks are mostly of the same parity as the ground state of the nucleus, with angular momenta differing at most by one unit. It can also be seen that most of the other states that significantly contribute to the cross sections are also of this type.

To further examine the nature of the strong cross section peaks in Figs. 9 and 10 it is appropriate to study the multipolarities of the corresponding transition operators. This has been done in Figs. 11 and 12 for ^{127}I and in Figs. 13 and 14 for ^{133}Cs, including only the leading multipole transitions. In Figs. 11 and 13 the multipole transitions have been

TABLE V. Average neutrino energies used in this paper and the corresponding neutrino temperatures (MeV).

	ν_e	$\overline{\nu}_e$	$\nu_x/\overline{\nu}_x$
$\langle E \rangle$	11.5	13.6	16.3
$T_{\alpha=0}$	3.65	4.32	5.17
$T_{\alpha=3}$	2.88	3.41	4.08

TABLE VI. CL and T contributions of Eqs. (16) and (17), along with contributions from terms of different tensorial properties (V, A, and I), to the total elastic folded neutrino-scattering cross section for ^{127}I (from reference nuclei ^{126}Te and ^{128}Xe) and ^{133}Cs (from reference nuclei ^{132}Xe and ^{134}Ba) in units of 10^{-44} cm^2. The format in which the data are presented is the same as in Table IV.

	^{127}I				^{133}Cs			
	ν_e	ν_x	$\overline{\nu}_e$	$\overline{\nu}_x$	ν_e	ν_x	$\overline{\nu}_e$	$\overline{\nu}_x$
$CL_{\alpha=0}$	(3.23,3.21)(5)	(5.90,5.88)(5)	(4.34,4.33)(5)	(5.90,5.88)(5)	(3.58,3.57)(5)	(6.54,6.52)(5)	(4.82,4.81)(5)	(6.54,6.52)(5)
$CL_{\alpha=3}$	(3.06,3.05)(5)	(5.71,5.68)(5)	(4.15,4.14)(5)	(5.71,5.68)(5)	(3.40,3.39)(5)	(6.33,6.31)(5)	(4.61,4.60)(5)	(6.33,6.31)(5)
$T_{\alpha=0}$	(3.82,3.89)(1)	(6.43,6.55)(1)	(3.87,3.95)(1)	(4.82,4.91)(1)	(2.06,2.14)(1)	(3.27,3.41)(1)	(2.16,2.24)(1)	(2.63,2.73)(1)
$T_{\alpha=3}$	(3.71,3.78)(1)	(6.46,6.58)(1)	(3.90,3.97)(1)	(4.95,5.04)(1)	(2.03,2.11)(1)	(3.37,3.50)(1)	(2.20,2.28)(1)	(2.74,2.85)(1)
$V_{\alpha=0}$	(3.23,3.21)(5)	(5.90,5.88)(5)	(4.34,4.33)(5)	(5.90,5.88)(5)	(3.58,3.57)(5)	(6.54,6.52)(5)	(4.82,4.81)(5)	(6.54,6.52)(5)
$V_{\alpha=3}$	(3.06,3.05)(5)	(5.71,5.68)(5)	(4.15,4.13)(5)	(5.71,5.68)(5)	(3.40,3.39)(5)	(6.33,6.31)(5)	(4.61,4.60)(5)	(6.33,6.31)(5)
$A_{\alpha=0}$	(5.48,5.58)(1)	(9.37,9.56)(1)	(7.17,7.30)(1)	(9.39,9.56)(1)	(3.11,3.23)(1)	(5.27,5.47)(1)	(4.05,4.20)(1)	(5.27,5.47)(1)
$A_{\alpha=3}$	(5.30,5.39)(1)	(9.31,9.48)(1)	(7.01,7.14)(1)	(9.31,9.48)(1)	(3.02,3.13)(1)	(5.25,5.45)(1)	(3.98,4.13)(1)	(5.25,5.45)(1)
$I_{\alpha=0}$	(3.71,3.78)(0)	(8.04,8.19)(0)	(−5.47, −5.57)(0)	(−8.04, −8.19)(0)	(1.61,1.68)(0)	(3.22,3.37)(0)	(−2.29, −2.39)(0)	(−3.22, −3.37)(0)
$I_{\alpha=3}$	(3.30,3.36)(0)	(7.54,7.68)(0)	(−4.98, −5.07)(0)	(−7.54, −7.68)(0)	(1.46,1.52)(0)	(3.15,3.28)(0)	(−2.15, −2.25)(0)	(−3.15, −3.28)(0)
$Total_{\alpha=0}$	(3.23,3.21)(5)	(5.90,5.88)(5)	(4.34,4.33)(5)	(5.90,5.88)(5)	(3.58,3.57)(5)	(6.54,6.52)(5)	(4.82,4.81)(5)	(6.54,6.52)(5)
$Total_{\alpha=3}$	(3.06,3.05)(5)	(5.71,5.68)(5)	(4.15,4.14)(5)	(5.71,5.68)(5)	(3.40,3.39)(5)	(6.33,6.31)(5)	(4.61,4.60)(5)	(6.33,6.31)(5)

TABLE VII. CL and T contributions of Eqs. (16) and (17), along with contributions from terms of different tensorial properties (V, A, and I), to the total inelastic folded neutrino scattering cross section for ^{127}I (from reference nuclei ^{126}Te and ^{128}Xe) and ^{133}Cs (from reference nuclei ^{132}Xe and ^{134}Ba) in units of 10^{-43} cm^2. The format in which the data are presented is the same as in Table IV.

	^{127}I				^{133}Cs			
	ν_e	ν_x	$\overline{\nu}_e$	$\overline{\nu}_x$	ν_e	ν_x	$\overline{\nu}_e$	$\overline{\nu}_x$
$CL_{\alpha=0}$	(9.65,8.25)(0)	(3.38,3.05)(1)	(1.79,1.58)(1)	(3.38,3.05)(1)	(8.60,7.94)(0)	(3.01,2.83)(1)	(1.59,1.48)(1)	(3.01,2.83)(1)
$CL_{\alpha=3}$	(6.82,5.65)(0)	(2.55,2.24)(1)	(1.31,1.11)(1)	(2.55,2.24)(1)	(6.04,5.53)(0)	(2.26,2.10)(1)	(1.16,1.07)(1)	(2.26,2.10)(1)
$T_{\alpha=0}$	(4.93,4.52)(1)	(1.66,1.61)(2)	(7.68,7.29)(1)	(1.37,1.33)(2)	(4.72,4.21)(1)	(1.63,1.47)(2)	(7.67,6.83)(1)	(1.38,1.24)(2)
$T_{\alpha=3}$	(3.47,3.06)(1)	(1.30,1.23)(2)	(5.83,5.37)(1)	(1.10,1.05)(2)	(3.25,2.88)(1)	(1.26,1.13)(2)	(5.76,5.11)(1)	(1.11,9.85)(2,1)
$V_{\alpha=0}$	(5.36,3.92)(0)	(2.33,1.94)(1)	(1.11,8.67)(1,0)	(2.33,1.94)(1)	(4.20,3.96)(0)	(1.97,1.89)(1)	(9.04,8.59)(0)	(1.97,1.89)(1)
$V_{\alpha=3}$	(3.33,2.20)(0)	(1.56,1.22)(1)	(7.11,5.13)(0)	(1.56,1.22)(1)	(2.45,2.30)(0)	(1.28,1.21)(1)	(5.53,5.20)(0)	(1.28,1.21)(1)
$A_{\alpha=0}$	(5.02,4.66)(1)	(1.62,1.58)(2)	(9.05,8.63)(1)	(1.62,1.58)(2)	(4.90,4.37)(1)	(1.61,1.45)(2)	(8.92,7.97)(1)	(1.61,1.45)(2)
$A_{\alpha=3}$	(3.62,3.24)(1)	(1.30,1.24)(2)	(6.87,6.35)(1)	(1.30,1.24)(2)	(3.46,3.07)(1)	(1.28,1.15)(2)	(6.71,5.97)(1)	(1.28,1.15)(2)
$I_{\alpha=0}$	(3.33,2.92)(0)	(1.46,1.39)(1)	(−6.89, −6.31)(0)	(−1.46, −1.39)(1)	(2.59,2.37)(0)	(1.25,1.15)(1)	(−5.63, −5.17)(0)	(−1.25, −1.15)(1)
$I_{\alpha=3}$	(2.05,1.69)(0)	(9.75,8.90)(0)	(−4.42, −3.84)(0)	(−9.75, −8.90)(0)	(1.49,1.36)(0)	(7.93,7.27)(0)	(−3.40, −3.11)(0)	(−7.93, −7.27)(0)
$Total_{\alpha=0}$	(5.89,5.34)(0)	(2.00,1.91)(2)	(9.47,8.87)(1)	(1.71,1.64)(2)	(5.58,5.00)(1)	(1.93,1.75)(2)	(9.26,8.31)(1)	(1.68,1.52)(2)
$Total_{\alpha=3}$	(4.16,3.63)(1)	(1.55,1.45)(2)	(7.14,6.48)(1)	(1.36,1.27)(2)	(3.85,3.44)(1)	(1.49,1.34)(2)	(6.92,6.18)(1)	(1.33,1.19)(2)

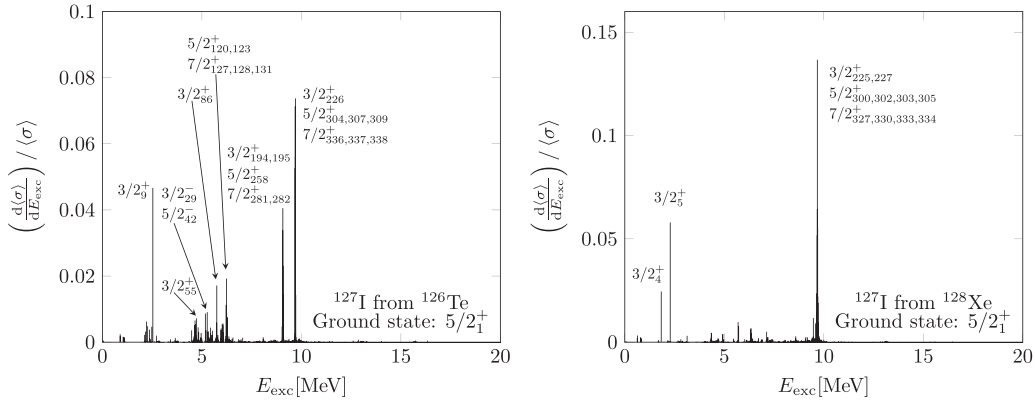

FIG. 9. Contributions to the total folded inelastic differential electron-neutrino cross section from different nuclear final states for ^{127}I obtained by using MQPM reference nuclei ^{126}Te (left) and ^{128}Xe (right), with the degeneracy parameter choice $\alpha = 3.0$, normalized to the total folded cross section. Individual states that have a contribution of at least $>10\%$ of the contribution of the individual state with the largest contribution have been labeled according to their quantum numbers J^π_n, where J^π is the spin parity of the state, and n is a quantum number that enumerates the states of that spin parity from the lowest energy to the highest.

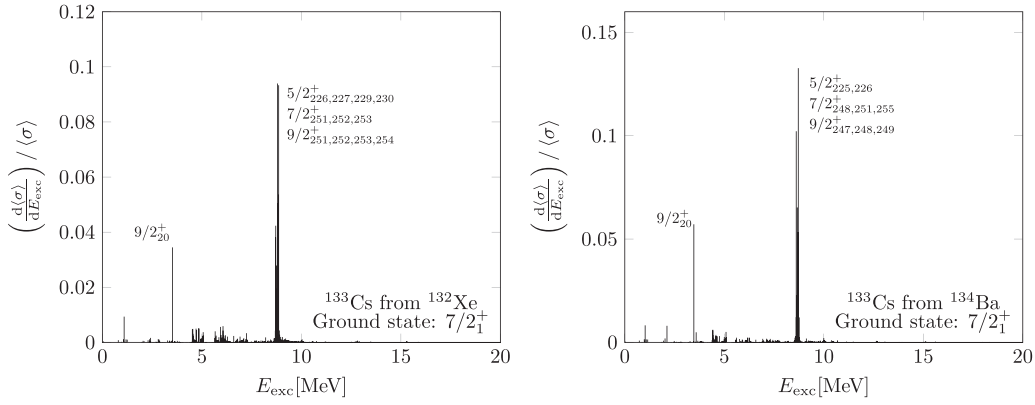

FIG. 10. Contributions to the total folded inelastic differential electron-neutrino cross section from different nuclear final states for ^{133}Cs obtained by using MQPM reference nuclei ^{132}Xe (left) and ^{134}Ba (right), with the degeneracy parameter choice $\alpha = 3.0$, normalized to the total folded cross section. Individual states have been labeled in the same manner as in Fig. 9.

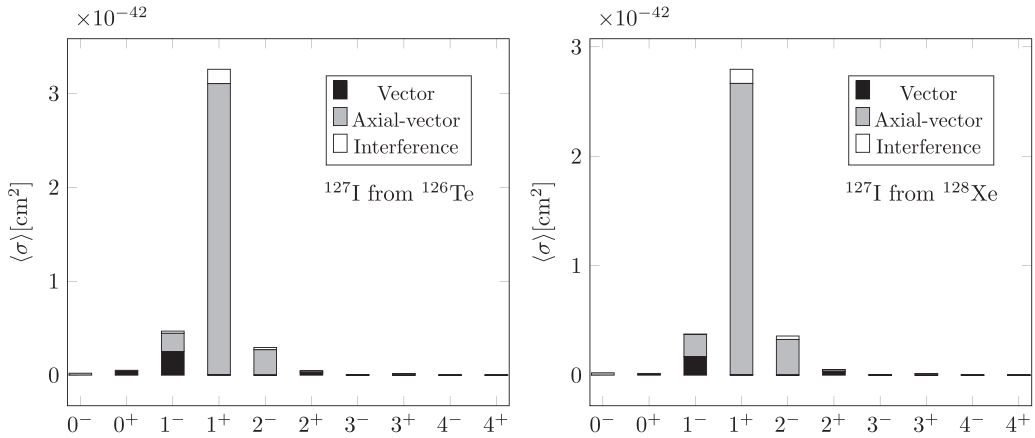

FIG. 11. Vector, axial-vector, and interference contributions to the total folded inelastic electron-neutrino cross section from the lowest ($J \leqslant 4$) multipole channels for supernova neutrino scattering off ^{127}I with $\alpha = 3.0$. The MQPM reference nuclei used were ^{126}Te (left) and ^{128}Xe (right).

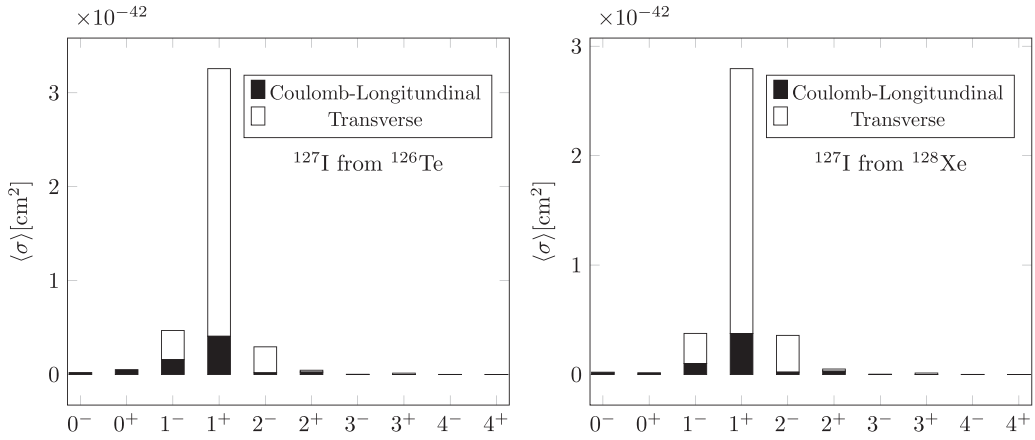

FIG. 12. Coulomb-longitudinal and transverse contributions to the total folded inelastic electron-neutrino cross section from the lowest ($J \leqslant 4$) multipole channels for supernova neutrino scattering off ^{127}I with $\alpha = 3.0$. The MQPM reference nuclei used were ^{126}Te (left) and ^{128}Xe (right).

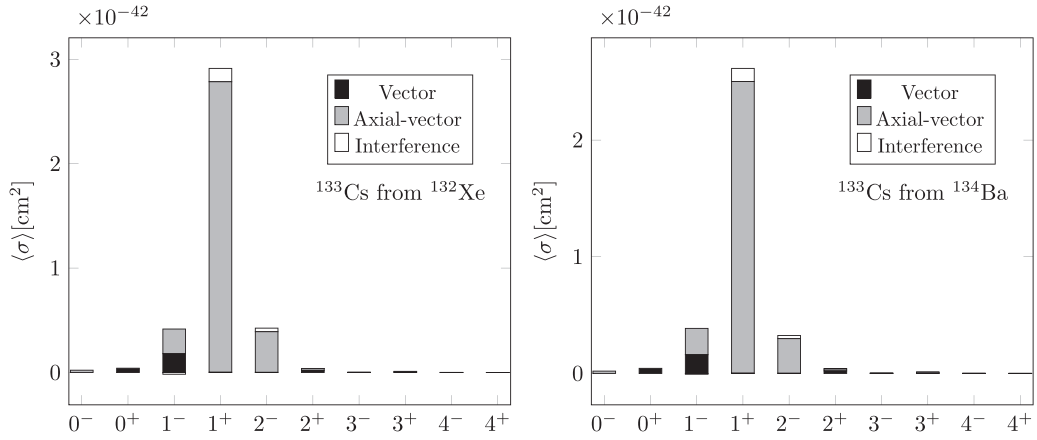

FIG. 13. Vector, axial-vector, and interference contributions to the total folded inelastic electron-neutrino cross section from the lowest ($J \leqslant 4$) multipole channels for supernova neutrino scattering off ^{133}Cs with $\alpha = 3.0$. The MQPM reference nuclei used were ^{132}Xe (left) and ^{134}Ba (right).

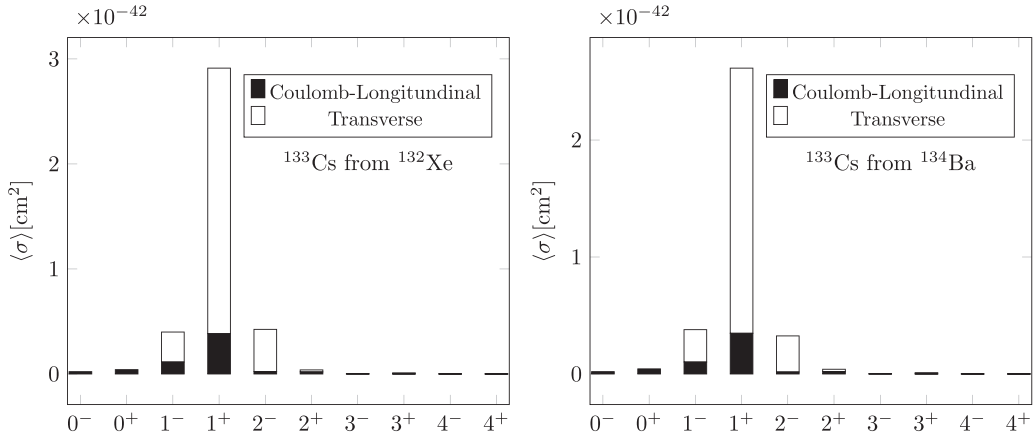

FIG. 14. Coulomb-longitudinal and transverse contributions to the total folded inelastic electron-neutrino cross section from the lowest ($J \leqslant 4$) multipole channels for supernova neutrino scattering off ^{133}Cs with $\alpha = 3.0$. The MQPM reference nuclei used were ^{132}Xe (left) and ^{134}Ba (right).

broken down to vector, axial-vector, and interference contributions, whereas in Figs. 12 and 14 they are divided in the Coulomb-longitudinal [see Eq. (16)] and transverse [see Eq. (17)] contributions. It can be seen in the figures that the 1^+ multipole dominates and it is of axial-vector type, mediated by a magnetic type of an operator in the transverse part (17) of the cross section. This indicates that the "culprit" is the Pauli spin operator and the strong peaks in the scattering cross section correspond to the M1 type of transition strength. This, in turn, means that the strong excitation peaks above 8 MeV in Figs. 9 and 10 correspond to spin-flip M1 giant resonances (see, e.g., [73]).

IV. CONCLUSIONS

In this paper we have briefly reviewed the theory behind the QRPA and MQPM and the formalism of neutral-current neutrino-nucleus scattering. We have constructed the MQPM wave functions for the nuclei ^{127}I and ^{133}Cs using two feasible even-even reference nuclei for both nuclei, for states up to $\approx$27 MeV in energy. We applied the presented scattering formalism and computed the scattering cross sections as a function of energy for both elastic and inelastic scattering and all flavors of (anti)neutrinos. These results can be of use to experimentalists working with detectors where iodine and cesium are present, as the cross sections can be folded over the energy spectra of the neutrinos considered in the experiments.

It was found that the elastic cross sections were orders of magnitude higher than the corresponding inelastic cross sections, as expected. For both odd nuclei the differences between results from different MQPM reference nuclei were reasonable for inelastic scattering and almost negligible for elastic scattering. The elastic cross sections were found to be roughly proportional to the square of the mass number of the nucleus for all neutrino energies in the case of both electron neutrinos and electron antineutrinos. The inelastic cross sections, on the other hand, were found to be more dependent on the nucleus considered and less on the neutrino type for low (anti)neutrino energies. This trend reversed for high (anti)neutrino energies.

We used the obtained cross section results to compute the energy-averaged cross section for neutral-current scattering of supernova neutrinos by folding the results with a pinched Fermi-Dirac spectrum. The folded cross sections were found to be moderately sensitive to the neutrino temperature, and conclusions similar to the unfolded results were drawn on the differences between the results from different MQPM reference nuclei. We also discussed the contributions to the total folded cross sections for electron-neutrino scattering from individual final nuclear states. A considerable fraction of the contributions was found to originate from peaklike structures of small width, composed of a relatively small number of strong contributions, at energies between 8 and 10 MeV. The different decompositions of these strong peaks revealed that they mostly correspond to magnetic axial-vector-type transitions of multipolarity 1^+, leading us to believe that they constitute spin-flip M1 giant resonances.

ACKNOWLEDGMENTS

This work has been partially supported by the Academy of Finland under Project No. 318043. M.H. acknowledges financial support from the Väisälä Foundation.

[1] T. Suzuki and T. Kajino, J. Phys. G **40**, 083101 (2013).
[2] T. Kajino, G. J. Mathews, and T. Hayakawa, J. Phys. G **41**, 044007 (2014).
[3] H. A. Bethe, Rev. Mod. Phys. **62**, 801 (1990).
[4] H. T. Janka, K. Langanke, A. Marek, G. Martiínez-Pinedo, and P. Müller, Phys. Rep. **442**, 38 (2007).
[5] H. T. Janka, Annu. Rev. Nucl. Part. Sci. **62**, 407 (2012).
[6] G. G. Raffelt, Annu. Rev. Nucl. Part. Sci. **49**, 163 (1999).
[7] G. G. Raffelt, Prog. Part. Nucl. Phys. **64**, 393 (2010).
[8] A. B. Balantekin and G. M. Fuller, J. Phys. G **29**, 2513 (2003).
[9] K. Scholberg, Annu. Rev. Nucl. Part. Sci. **62**, 81 (2012).
[10] K. Langanke and E. Kolbe, At. Data Nucl. Data Tables **79**, 293 (2001).
[11] K. Langanke and G. Martiínez-Pinedo, Rev. Mod. Phys. **75**, 819 (2003).
[12] H. Ejiri, Phys. Rep. **338**, 265 (2000).
[13] H. Ejiri, J. Suhonen, and K. Zuber, Phys. Rep. **797**, 1 (2019).
[14] K. Scholberg, AIP Conf. Proc. **1666**, 070002 (2015).
[15] P. Antonioli *et al.*, New J. Phys. **6**, 114 (2004).
[16] S. Fukuda *et al.* (Super-Kamiokande Collaboration), Nucl. Instrum. Methods Phys. Res., Sect. A **501**, 418 (2003).
[17] M. Aglietta *et al.* (LVD Collaboration), Il Nuovo Cimento A **105**, 1793 (1992).
[18] R. Abbasi *et al.* (IceCube Collaboration), Nucl. Instrum. Methods Phys. Res., Sect. A **601**, 294 (2009).
[19] S. Abe *et al.* (KamLAND Collaboration), Phys. Rev. C **81**, 025807 (2010).
[20] G. Alimonti *et al.* (Borexino Collaboration), Nucl. Instrum. Methods Phys. Res., Sect. A **600**, 568 (2009).
[21] C. A. Duba *et al.*, J. Phys.: Conf. Ser. **136**, 042077 (2008).
[22] S. Adrián-Martínez *et al.* (KM3NeT Collaboration), J. Phys. G **43**, 084001 (2016).
[23] Y. Wang, Phys. Procedia **37**, 22 (2012).
[24] B. Dutta and L. E. Strigari, Annu. Rev. Nucl. Part. Sci. **69**, 137 (2019).
[25] H. S. Lee *et al.* (KIMS Collaboration), Phys. Lett. B **633**, 201 (2005).
[26] D. Akimov *et al.* (COHERENT Collaboration), Science **357**, 1123 (2017).
[27] P. Adhikari *et al.* (KIMS Collaboration), Eur. Phys. J. C **76**, 185 (2016).
[28] R. Bernabei *et al.* (DAMA/LIBRA Collaboration), Universe **4**, 116 (2018).
[29] E. Barbosade de Souza *et al.* (DM-Ice Collaboration), Phys. Rev. D **95**, 032006 (2017).
[30] K. Fushimi *et al.* (PICO-LON Collaboration), J. Phys. G. Conf. Series **718**, 042022 (2016).

[31] J. Xu, F. Calaprice, F. Froborg, E. Shields, and B. Suerfu (SABRE Collaboration), in *Low Radioactivity Techniques 2015 (LRT 2015): Proceedings of the 5th International Workshop in Low Radioactivity Techniques*, edited by J. L. Orrell, AIP Conf. Proc. No. 1672 (AIP, New York, 2015), p. 040001.
[32] J. Amaré *et al.* (ANAIS Collaboration), Phys. Rev. Lett. **123**, 031301 (2019).
[33] M.-K. Cheoun, E. Ha, K. S. Kim, and T. Kajino, J. Phys. G **37**, 055101 (2010).
[34] H. Dapo and N. Paar, Phys. Rev. C **86**, 035804 (2012).
[35] E. Kolbe and K. Langanke, Phys. Rev. C **63**, 025802 (2001).
[36] T. Suzuki, M. Honma, K. Higashiyama, T. Yoshida, T. Kajino, T. Otsuka, H. Umeda, and K. Nomoto, Phys. Rev. C **79**, 061603(R) (2009).
[37] A. A. Dzhioev, A. I. Vdovin, G. Martínez-Pinedo, J. Wambach, and Ch. Stoyanov, Phys. Rev. C **94**, 015805 (2016).
[38] V. Tsakstara and T. S. Kosmas, Phys. Rev. C **86**, 044618 (2012).
[39] M.-K. Cheoun, E. Ha, T. Hayakawa, S. Chiba, K. Nakamura, T. Kajino, and G. J. Mathews, Phys. Rev. C **85**, 065807 (2012).
[40] E. Ydrefors, K. G. Balasi, J. Suhonen, and T. S. Kosmas, in *Neutrinos: Properties, Sources and Detection*, edited by J. P. Greene (Nova Science, New York, 2011), pp. 151–175.
[41] E. Ydrefors, K. G. Balasi, T. S. Kosmas, and J. Suhonen, Nucl. Phys. A **866**, 67 (2011).
[42] K. G. Balasi, E. Ydrefors, and T. S. Kosmas, Nucl. Phys. A **868-869**, 82 (2011).
[43] E. Ydrefors, K. G. Balasi, T. S. Kosmas, and J. Suhonen, Nucl. Phys. A **896**, 1 (2012).
[44] E. Ydrefors and W. Almosly, Rom. J. Phys. **60**, 836 (2015).
[45] W. Almosly, E. Ydrefors, and J. Suhonen, J. Phys. G **40**, 095201 (2013); **42**, 025106 (2015).
[46] V. Tsakstara and T. S. Kosmas, Phys. Rev. C **83**, 054612 (2011).
[47] E. Ydrefors, J. Suhonen, and Y. M. Zhao, Phys. Rev. C **91**, 014307 (2015).
[48] P. Pirinen, E. Ydrefors, and J. Suhonen, Adv. High Energy Phys. **2018**, 9163586 (2018).
[49] M.-K. Cheoun, E. Ha, T. Hayakawa, T. Kajino, and S. Chiba, Phys. Rev. C **82**, 035504 (2010).
[50] D. Gazit and N. Barnea, Phys. Rev. C **70**, 048801 (2004).
[51] T. Suzuki, S. Chiba, T. Yoshida, T. Kajino, and T. Otsuka, Phys. Rev. C **74**, 034307 (2006).
[52] N. Jachowicz, S. Rombouts, K. Heyde, and J. Ryckebusch, Phys. Rev. C **59**, 3246 (1999).
[53] A. Bortugno and G. Co', Nucl. Phys. A **761**, 200 (2005).
[54] M.-K. Cheoun, E. Ha, and T. Kajino, Phys. Rev. C **83**, 028801 (2011).
[55] J. Engel, G. C. McLaughlin, and C. Volpe, Phys. Rev. D **67**, 013005 (2003)
[56] O. Civitarese and T. Tarutina, Phys. Rev. C **94**, 054603 (2016).
[57] W. Almosly, B. G. Carlsson, J. Suhonen, and E. Ydrefors, Phys. Rev. C **99**, 055801 (2019).
[58] J. Toivanen and J. Suhonen, J. Phys. G **21**, 1491 (1995); Phys. Rev. C **57**, 1237 (1998).
[59] A. Bohr and B. R. Mottelson, *Nuclear Structure* (Benjamin, New York, 1969), Vol. 1.
[60] J. Suhonen, *From Nucleons to Nucleus: Concepts of Microscopic Nuclear Theory* (Springer-Verlag, Berlin, 2007).
[61] J. Suhonen, A. Faessler, T. Taigel, and T. Tomoda, Phys. Lett. B **202**, 174 (1988).
[62] J. Suhonen, T. Taigel, and A. Faessler, Nucl. Phys. A **486**, 91 (1988).
[63] J. Katakura and K. Kitao, Nucl. Data Sheets **97**, 765 (2002).
[64] Z. Elekes and J. Timar, Nucl. Data Sheets **129**, 191 (2005).
[65] Yu. Khazov, A. A.Rodionov, S. Sakharov, and B. Singh, Nucl. Data Sheets **104**, 497 (2005).
[66] A. A. Sonzogni, Nucl. Data Sheets **103**, 1 (2004).
[67] A. Hashizume, Nucl. Data Sheets **112**, 1647 (2011).
[68] Y. Khazov, A. Rodionov, and F. Kondev, Nucl. Data Sheets **112**, 855 (2011).
[69] T. W. Donnelly and R. D. Peccei, Phys. Rep. **50**, 1 (1979).
[70] J. D. Walecka, *Theoretical Nuclear and Subnuclear Physics* (Imperial College, London, 2004).
[71] H.-T. Janka and W. Hillebrandt, Astron. Astrophys. Suppl. Ser. **78**, 375 (1989).
[72] M. T. Keil and G. G. Raffelt, Astrophys. J. **590**, 971 (2003).
[73] V. O. Nesterenko, J. Kvasil, P. Vesely, W. Kleinig, and P.-G. Reinhard, J. Phys. G **37**, 064034 (2010).